3D printer-driven design of a non-assembly titanium surgical instrument using compliant lattice flexures

Lussenburg, Kirsten; van Starkenburg, Remi; Sakes, Aimée; Breedveld, Paul

DOI
10.1016/j.matdes.2024.112845

Publication date
2024

Document Version
Final published version

Published in
Materials and Design

Citation (APA)
Lussenburg, K., van Starkenburg, R., Sakes, A., & Breedveld, P. (2024). 3D printer-driven design of a non-assembly titanium surgical instrument using compliant lattice flexures. *Materials and Design*, *240*, Article 112845. https://doi.org/10.1016/j.matdes.2024.112845

Materials & Design 240 (2024) 112845

Contents lists available at ScienceDirect

Materials & Design

journal homepage: www.elsevier.com/locate/matdes

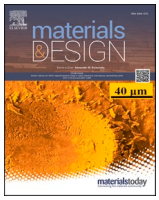

3D printer-driven design of a non-assembly titanium surgical instrument using compliant lattice flexures

Kirsten Lussenburg [a,*], Remi van Starkenburg [b], Aimée Sakes [a], Paul Breedveld [a]

[a] Bio-Inspired Technology Group (BITE), Department BioMechanical Engineering, Faculty of Mechanical, Maritime, and Materials Engineering, Delft University of Technology, The Netherlands
[b] Department of Electronic and Mechanical Support Division (DEMO), Delft University of Technology, The Netherlands

ARTICLE INFO

Keywords:
Selective laser melting
Non-assembly
Lattice
Compliant
Surgical instrument

ABSTRACT

Metal additive manufacturing is a promising technology for the production of functional medical products, due to its high shape complexity and resolution, and ability to withstand sterilization temperatures. This study explores the possibility of designing a completely non-assembly steerable surgical instrument using Selective Laser Melting. Despite its advantages for medical devices, the rough surface quality of unfinished parts can be problematic for non-assembly designs, leading to increased friction and wear in rigid body mechanisms and tendon-actuated mechanisms. We investigated printing of rolling contact joints with crossed flexures as low-friction joints, adjusted for printing in titanium for the design of the instrument. Grid-based lattice structures were incorporated as miniature flexures, and we explored the influence of various grid sizes on the flexibility and bending stiffness of the lattices. Based on this exploration, we altered the rolling joint configuration from two crossed flexures to a single straight flexure for our design. The resulting steerable surgical instrument design is completely non-assembly, including its actuation, facilitates easy removal of support structures, and requires no surface finishing steps. It has a diameter of less than 20 mm, facilitates opening and closing of a grasper, and steering of the grasper by 20 degrees.

1. Introduction

1.1. Additive manufacturing

Additive manufacturing (AM) or 3D printing has emerged as a promising technology for the production of functional, medical products. It has been applied in a number of medical fields, among which personalized implants, anatomical models, surgical guides, prostheses, and surgical instruments [1]. 3D printed medical products can reduce surgical time and improve medical outcomes [2]. The ability to create highly complex parts makes it possible to create personalized medical products for both patient and surgeon, as well as for advanced functionalities in terms of usability. In addition, AM enables the creation of non-assembly designs, which are functional mechanisms that can be produced in a single production step [3]. Non-assembly designs have some advantages over traditional assembly-based designs, as they reduce the processing time and costs, and allow for an increase in complexity of the design. In the medical field, non-assembly designs enable the creation of increasingly complex devices that can facilitate a wide range of complex operations.

The most widely utilized AM technologies in the medical domain are those that use polymers as a base material [1]. While many polymer-based AM technologies have been explored for medical designs, these materials are often challenging to sterilize and often suffer from poor mechanical properties. Therefore, for some medical applications, metals are preferred over polymers, because of their high stiffness, biocompatibility, and ability to withstand high temperatures during the sterilization process [4]. Metal AM processes, described by the umbrella term Selective Laser Melting (SLM), allow for the production of components with a high shape complexity and resolution. This makes the process ideal for the production of medical and surgical instruments, which can benefit from the advantages of SLM to produce complex, personalized instruments at lower costs as compared to conventional manufacturing for small batch sizes [5]. So far, medical applications of SLM include customized implants [6,7], surgical guides [8], forceps [9,10], surgical clamps [11], grasper jaws [12,13], and (parts of) steerable surgical

* Corresponding author.
E-mail addresses: k.m.lussenburg@tudelft.nl (K. Lussenburg), r.i.b.vanstarkenburg@tudelft.nl (R. van Starkenburg), a.sakes@tudelft.nl (A. Sakes), p.breedveld@tudelft.nl (P. Breedveld).

https://doi.org/10.1016/j.matdes.2024.112845
Received 12 December 2023; Received in revised form 19 February 2024; Accepted 10 March 2024
Available online 12 March 2024

instruments [5,14,15].

Although SLM shows many advantages for the production of medical devices, unfinished parts have a rough surface quality that can be problematic for use in non-assembly designs. Especially in mechanisms with interacting surfaces, such as rigid body joints and mechanisms actuated by tendons, a rough surface finish increases friction and wear and can hinder the operation of the mechanism [16]. The influence of a rough surface finish is even more noticeable for small or miniaturized parts, where geometrical feature sizes are only a few times larger than the size of the metal particles. One way to improve the surface quality of SLM parts is by employing industrial surface finishing techniques, such as grinding or mechanical polishing [17,18]. However, in non-assembly designs mechanical surfaces are often inaccessible by these techniques, since the designs cannot be disassembled to allow for easy access to the inner geometry [19]. Thus, while SLM-based non-assembly designs may reduce production time and costs, the complex post-processing required can offset these gains.

1.2. Steerable surgical instruments

Medical non-assembly mechanisms are particularly promising for the production of instruments with steerable end-effectors. Current surgical practices have seen a shift from open surgery to minimally invasive surgery (MIS), in which only three small incisions are required instead of one large incision. Conventional surgical instruments, consisting of a handle, straight shaft, and rigid end-effector, severely reduce the dexterity of the surgeon in MIS, due to restrictions posed by the small incision size. In response, steerable end-effectors have been developed [20–24], which provide the surgeon with additional degrees of freedom (DOF), without sacrificing the advantages of small incision sizes. Steerable instruments usually consist of many small, complex parts that provide the end-effector with the additional DOF. Non-assembly AM is a promising approach to increase the speed and ease of production of these miniature devices.

Steerable end-effectors usually rely on tendon-actuation, which is a cheap and efficient choice, since tendons require little space and can be easily embedded in various designs due to their high tensile strength and flexibility. However, in non-assembly designs, tendons have to be inserted into the designs after printing, since current AM technologies are less suited to 3D print long, thin, flexible structures with a high tensile strength. Accurately inserting tendons in a 3D printed device can be a considerably lengthy task that usually has to be performed manually [20]. Furthermore, it has proven difficult to precisely 3D print hollow small diameter channels through which the tendons are guided, due to the risk of them fusing shut, which hinders miniaturization of the instrument [21,25]. In the case of SLM, friction between the tendons and the rough surface of internal geometries inaccessible to surface finishing techniques can lead to premature failure of the tendons.

In this work, we describe the design and 3D print process for a steerable surgical instrument made of titanium, specifically tailored for the SLM process. Given the extensive design possibilities afforded by AM, which often can be challenging to implement and exploit, our approach involved a thorough analysis of the boundaries of the SLM process. This analysis allowed us to incorporate process-specific guidelines from the start, rather than after the conceptual design phase, establishing a framework we categorize as a 3D printer-driven design process. The resultant instrument design, which is completely non-assembly, including its actuation, facilitates easy removal of support structures and requires no surface finishing steps. As the instrument design was driven by the specifications of the SLM process, our design decisions were driven by the process specifications and design guidelines.

2. Materials and methods

2.1. Instrument requirements

Our main goal was to design a steerable instrument that does not require any assembly steps and a minimal number of post-processing steps. We define an assembly step as attaching two or more separate parts to each other by any means. The instrument has the following requirements:

1. **Actuation**: The actuation system of the instrument is completely 3D printed.
2. **Post-processing**: The only post-processing that we allowed is the unavoidable removal of the support structures.
3. **Friction**: Considering the rough surface of SLM parts, the instrument contains no sliding surfaces and is preferably entirely frictionless.
4. **Dimensions**: The maximum diameter of the instrument shaft is 20 mm. Although this is large considering the size of current surgical instruments, which typically have a diameter of less than 8 mm, it will give us more design freedom in this exploratory design without being hindered by SLM size limitations.
5. **Functionality**: The instrument should contain a grasper that can be opened with a maximum opening angle of 60°, and that can be steered by an angle of at least 45° with one DOF (planar bending).
6. **Material**: The instrument will be printed in titanium, because of its high stiffness and biocompatibility.

2.2. SLM design guidelines

The SLM process uses a thin layer of metal powder deposited for each layer, which is sintered by means of a focused laser beam. In this study, the SLM printer used is the Lasertec 30 SLM 2nd Gen (DMG Mori, Bielefeld, Germany), with a laser spot size of 73 μm and a 600 W laser unit. The metal powder used is Ti6Al4V grade 23 (Carpenter Additive, Widnes, United Kingdom). We comprised an inventory of design guidelines for SLM, which serve as foundation for the new design. The following list was drawn up from literature as well as from preliminary experiments with the used SLM printer. It should be noted that these values can differ depending on the specific 3D printer used and that they are often conservative estimates to ensure the successful printability of the part.

1. **Support structures:** Supports are required to anchor the workpiece to the base plate, for heat dissipation, and to reduce residual stresses [26]. Supports that are placed on flat surfaces reduce the complexity of support removal and result in a better surface finish than when removing them from a curved surface [26].
2. **Overhang:** To prevent the use of supports, features can be designed as 'self-supporting' when they have an overhang of less than 45° with respect to the build plate.
3. **Clearance:** Clearances between adjacent parts should be between 120 μm and 150 μm to prevent fusing of parts, depending on part orientation [27]. The same minimum size should be used for holes or channels.
4. **Wall thickness:** The reported minimum thickness of a solid, thin wall is approximately 0.4 mm for SLM [15,28], although for the 3D printer used in this study, the minimum wall thickness that could be obtained was 0.55 mm.
5. **Volume gradients:** The high thermal gradient of the metal powder can cause parts to warp or distort. Therefore, sudden increases in part volume should be avoided, to prevent small features from experiencing warpage or a modification in mechanical properties due to the radiant heat of the large volume.

2.3. Low friction joint design

Some studies have successfully 3D printed non-assembly rigid body joints using SLM [27,29–31], however, they require a relatively large clearance between the parts when printed in a pre-assembled position to prevent them from fusing [29]. This can hinder design scalability and miniaturization, and can result in excessive play when applied in a steerable mechanism. In addition, the functioning of rigid body joints can be hindered by friction from the rough surface finish of SLM. Therefore, the use of rigid body joints was excluded in our design, because these rely on sliding surfaces.

Rolling joints are examples of joints with low sliding friction, which do not require smooth polished surfaces. They consist of two bodies that are constrained by two or more flexures in a cross-linked configuration and roll over each other (Fig. 1a-b) [32–35]. The flexures allow the bodies of the joint to rotate with respect to each other without slipping, and as such, a low stiffness of the flexures is desired. Advantages of rolling joints are strongly reduced friction and wear on parts, large displacements, and no need for lubrication [32,33].

A number of steerable surgical instrument designs have incorporated rolling joints [34,36–38]. Jeanneau et al. [32] and Zhang et al. [36] 3D printed rolling joints using material extrusion and selective laser sintering, respectively. In both cases, the joint was printed with the flexures in a curved configuration, as shown in Fig. 1a, which means there is no stress in the flexures in the straight position [32]. However, to prevent fusing of the flexures to the joint body during printing, a gap had to be established between the flexures and the body, leading to backlash in the design [32]. Alternatively, the flexures can be printed in a straight configuration (Fig. 1c), as proposed by Halverson et al. [33]. This reduces the need for a gap, although the joint then needs to be placed in its curved position using an extra production step.

2.4. 3D printing of flexures

A rolling joint requires compliant flexures with a low stiffness. The stiffness of the flexures is limited by the minimum wall thickness that can be printed, which in our case is approximately 0.55 mm, resulting in rigid walls unsuitable for flexures. The wall thickness is affected by the underlying laser scan modes performed by the printer [39]. Different laser scan modes are used for different parts of the layer, i.e. the outer contour and the interior region, and settings can be adjusted accordingly. In Fig. 2a-b, the different laser scan modes for thick and thin walls are illustrated. For a thick wall (Fig. 2a), the laser first fills the interior region of the layer with a parallel hatch pattern, after which the outer contour is scanned with a single line. Since the melt pool of the laser is larger than the laser spot itself, the laser moves with an offset from the designed wall. For a thin wall (Fig. 2b), the laser only follows the contour of the wall, however, since there is not enough space to have the required offset, the melt pool of the laser spot will increase the wall thickness [40]. The influence of the melt pool can be controlled to a certain amount by parameters such as the scanning speed and laser wattage [39], however, these settings also affect the print quality. As such, reducing the wall thickness is in practice not feasible due to the internal printer settings.

Another way to decrease the wall stiffness is by using lattice structures, as recent studies have shown [41–44]. Advantages of lattice flexures are a reduced bending stiffness, a significantly lower mass, and good off-axis stiffness [41]. The SLM printer used in this study has a special slicing mode in the software for lattice structures. Using the lattice mode, the laser prints one voxel at a time, as illustrated in Fig. 2c, and only passes over the wall once. In this mode, the design of the lattice is completely 2-dimensional, therefore the thickness of the structure is purely determined by the laser spot size and printer settings. To develop the instrument, we further explored the possibility of using rolling joints in combination with lattice flexures.

2.5. Test parts

2.5.1. Lattice flexures

First, we explored the potential of 3D printed lattice flexures with different structures and lengths. The limitations of lattice mode are that the lattices can only be printed straight and perpendicular to the build plate, along the z-axis. We designed test parts as shown in Fig. 3a, consisting of a solid wall of 10 mm z-height and 1 mm thickness, interrupted by lattices with lengths of 10 mm and 25 mm. The lattices consist of a 2-dimensional grid, with cell sizes of 1 × 1 mm (L-1), 0.75 × 0.75 mm (L-0.75), 0.5 × 0.5 mm (L-0.5), 0.25 × 0.25 mm (L-0.25), and 0.05 × 0.05 mm (L-0.05) (not pictured). The lattices are constructed within the software of the SLM printer as dimensionless vectors based on an elementary cell. To define the cell, first, a cube is defined with x, y, and z values corresponding to the desired lattice grid size. For the first line a start point is defined at X0-Y0.5-Z0 and an end point at X1-Y0.5-Z1 (AB in Fig. 3b), for the second line the start point is defined as X0-Y0.5-Z0 and the end point as X1-Y0.5-Z1 (CD in Fig. 3b), together defining one cell of the grid. The software divides the vectors from start to finish in voxels, corresponding to one voxel per layer height. As such, the lattices are theoretically designed with no thickness, while in practice the thickness of the lattice will approach the size of the laser spot, including its melt pool, and be circular in shape. Since all the struts of the grid have an overhang angle of 45, they can be printed without requiring support structures. Each of the grid sizes was printed five times, resulting in a total of 25 test parts.

2.5.2. Rolling joint

We explored the feasibility of printing rolling joints with lattice flexures, by testing two design variables: the size of the joint and the structure of the lattice. The joints were printed in two halves with straight flexures, according to Fig. 1c. We introduced positive and negative form closures on the joint body to connect the bodies, as shown in Fig. 4a-b. The joints were designed with a diameter d of 10 mm, 7.5 mm, and 5 mm, with a z-height of 5 mm, 3.75 mm, and 2.5 mm respectively. The length of the flexure is directly related to the joint size

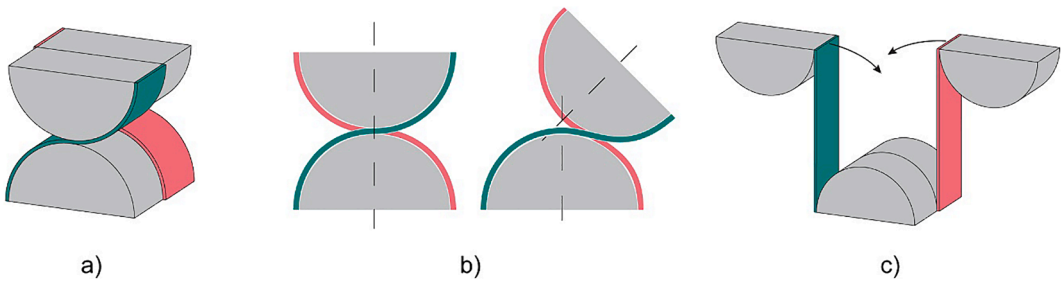

Fig. 1. Rolling joint with the two different flexures indicated in green and red. a) 3-dimensional view of a rolling joint. b) Side view of the rolling joint in neutral position and in bent configuration. c) Unfolded rolling joint with flexures in a straight position, the arrows indicate the folding direction. (For interpretation of the references to colour in this figure legend, the reader is referred to the web version of this article.)

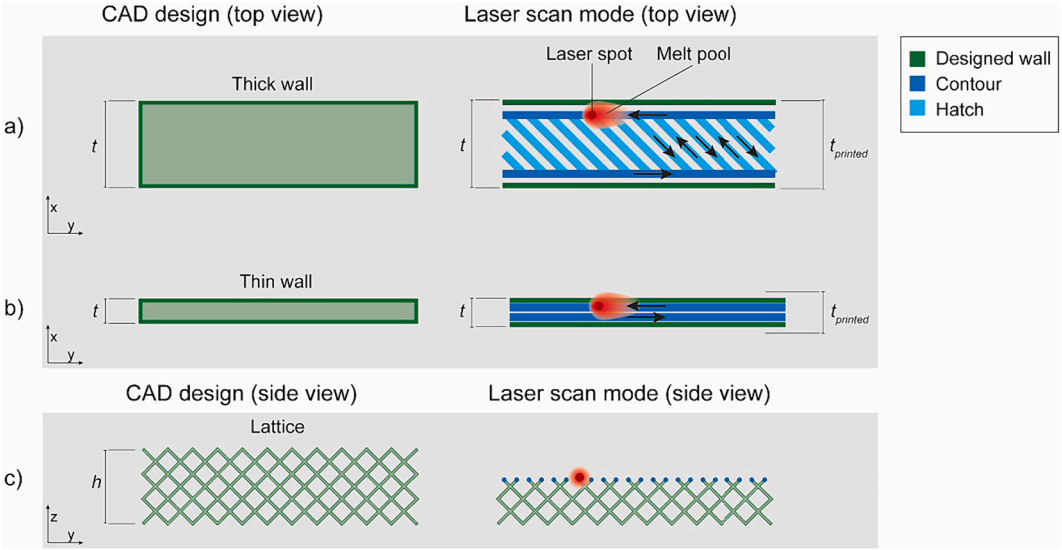

Fig. 2. Schematic overview of the different laser scan modes available for the 3D printer used in this study, in which t is the designed thickness of the wall and $t_{printed}$ the actual thickness of the printed wall. a) For a thick wall, the laser fills the interior region with a pattern called hatch, after which it follows the outer contour with an offset, resulting in a wall thickness similar to the designed wall. b) For a thin wall, only the contour is followed by the laser, which results in a wall thickness larger than designed due to the size of the laser melt pool. c) For a lattice wall, the laser only prints one point at a time.

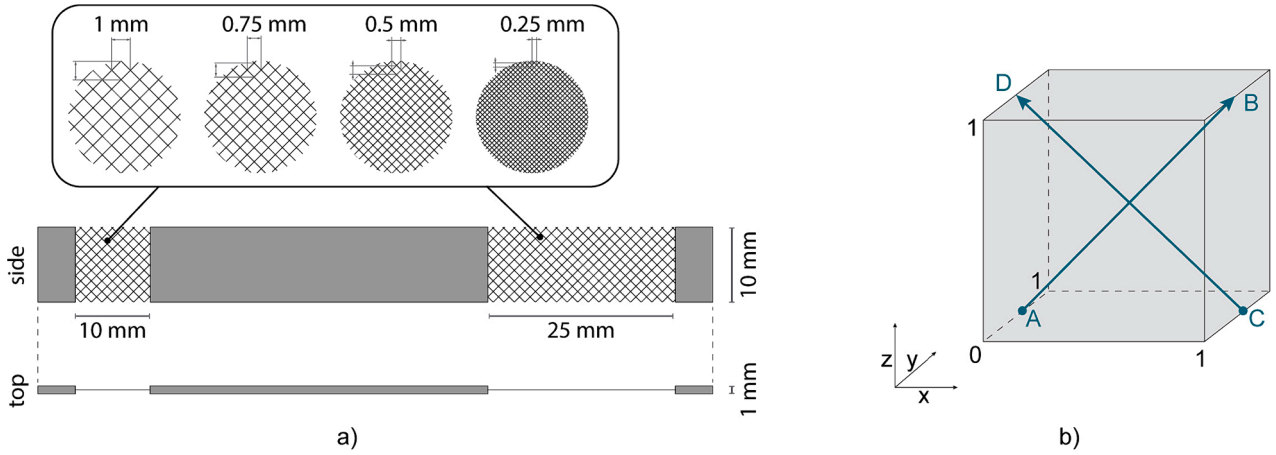

Fig. 3. Design of lattice test parts. a) Full test part, with lattice grid sizes of 1 × 1, 0.75 × 0.75, 0.5 × 0.5, 0.25 × 0.25 and 0.05 × 0.05 mm (not pictured). b) One lattice cell as designed in the software of the SLM printer, consisting of two dimensionless vectors AB and CD.

by $\frac{d}{2}\pi + c$, in which c is a clearance of 0.15 mm. All three sizes of the joints were printed with four lattice structures: L-1, L-0.75, L-0.5, and L-0.25 (12 full joints). In total three batches of joints were printed, resulting in a total of 36 full joints. In between the batches, the results were analyzed and revised where necessary.

2.6. Production

The used parameters of the SLM process are summarized in Table 1. All test parts were positioned with the lattices perpendicular to the movement of the wiper and in parallel with the argon flow.

Supports were removed using wire electrical discharge machining (wire EDM) (Fanuc, Oshino, Yamanashi, Japan) with 0.25 mm brass wire. Wire EDM can efficiently remove support structures in a straight line parallel to the build plate on the underside of the part in a single step, as long as all features are at the same distance from the build plate. The joints were positioned on the build plate with the form closures on top, so that supports on the bottom could easily be removed in a straight line. The joints were assembled by pushing the two joint bodies towards each other, thereby forcing the lattice to follow the radius of the body, and connecting the two halves with the form closure, as shown in Fig. 4b. Only one batch of the joints received a stress relief heat treatment at 850 °C for 2 h, after which the parts were cooled at room temperature.

2.7. Characterization

2.7.1. Dimensional accuracy

The wall thickness of the printed lattice flexures was measured using digital calipers, based on three measurements along the length of the flexure. The geometry and the strut sizes of the lattices were examined under a digital microscope (Dino-Lite 3.0, AnMo Electronics Corporation, Taiwan). We determined the theoretical and actual porosity of the lattices by isolating the 25 mm long lattice from the test parts after performing the other tests. Three lattices of each grid size were weighted on a calibrated scale, which was then divided by three to obtain their individual mass. For the theoretical porosity of the lattices, CAD-models of the structures were drawn in Solidworks (Dassault Systèmes, Paris, France), using a uniform strut diameter of 0.20 mm, and the mass of the

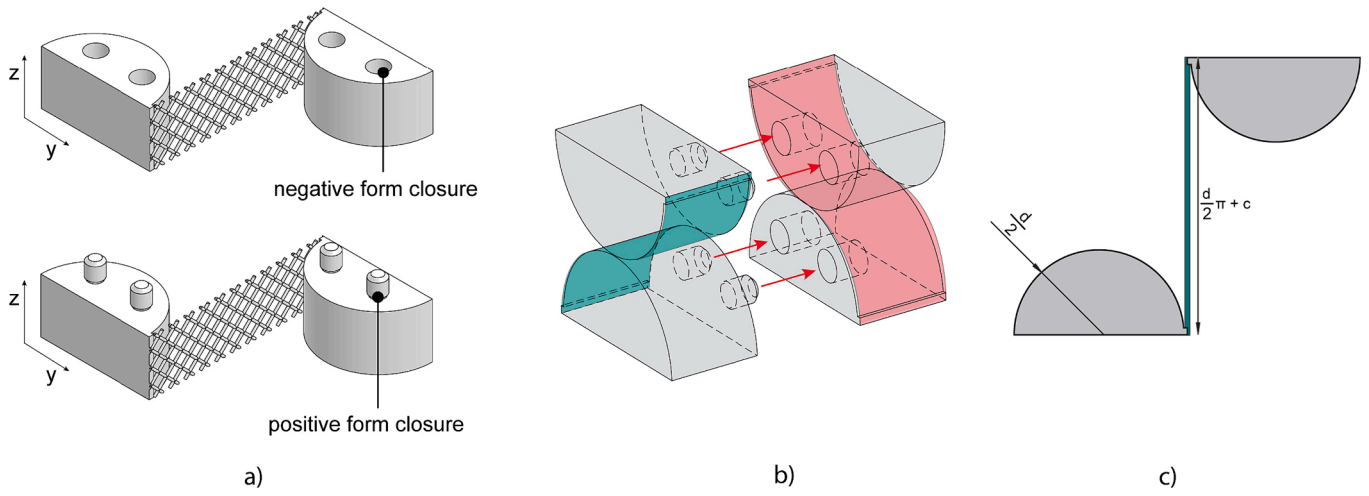

Fig. 4. Design of the rolling contact joint in its unfolded configuration. a) CAD model of the two joints showing the positive and negative form closure. b) Assembly of the positive and negative part. c) Side view of the joint with parameters, in which d is the diameter of the joint, t is the thickness of the lattice, and c is a clearance.

Table 1
Process parameters used in this study.

Layer height	50 µm			
	Scanning speed (mm/s)	Laser Power (Watt)	Hatch distance (mm)	Offset distance (mm)
Hatch	742	219	0.11	0.1
Contour	408	120	–	0.05
Lattice	1000	140	–	0

structures was determined using the 'Mass Properties' feature.

2.7.2. Bending performance

The lattice test parts were used to examine the bending stiffness of the different lattice structures, by measuring the deflection as a result of a calibrated force. Weights of 5 g, 10 g, 15 g, 20 g, 30 g, 40 g, 50 g, 60 g, 80 g, and 100 g were attached to both ends of the test parts subsequently while securing the middle part. The slope of the deflection of the lattice flexures was then measured using the digital microscope. The test setup is shown in Fig. 5. The test was repeated three times, using new test parts for each measurement.

When applied in the rolling joint, the lattice flexures should have a bending radius that corresponds to the diameter of the joint, i.e. 5 mm, 7.5 mm, or 10 mm. The bending radius of the lattices was evaluated by curving them over the joint body, if they were able to lay flat across the surface the bending radius suffices. After assembling the joint halves, the bending angle of the joints was evaluated. According to Requirement 5 in Section 2.1, the instrument should have a steering angle of at least 45°, however the design of the rolling joints allows a 90° bending angle in both directions. Therefore, we tested the rolling joints by manually bending them up to a 90° angle in both directions. We considered the joints successful if they were able to be assembled and bent without breaking and withstood bending at least 100 times.

3. Results

3.1. Flexures

All 25 lattice test parts printed successfully, however, some broke during the removal with wire EDM. From observations, we found that the lattices started to vibrate as a result of the wire EDM process, which led to a fracture originating from a small print defect. Therefore, only three test parts were tested per lattice structure. The 3D printed test parts are shown in Fig. 6a, along with microscope images of the different lattice structures (Fig. 6b-f). The microscope images show that L-1, L-0.75, and L-0.5 have a fairly regular pattern, whereas the denser L-0.25 and L-0.05 have no discernible print pattern, with only a few small gaps visible between the struts (light blue 'flecks' in Fig. 6e-f).

The wall thickness and strut size of the lattices are given in Table 2.

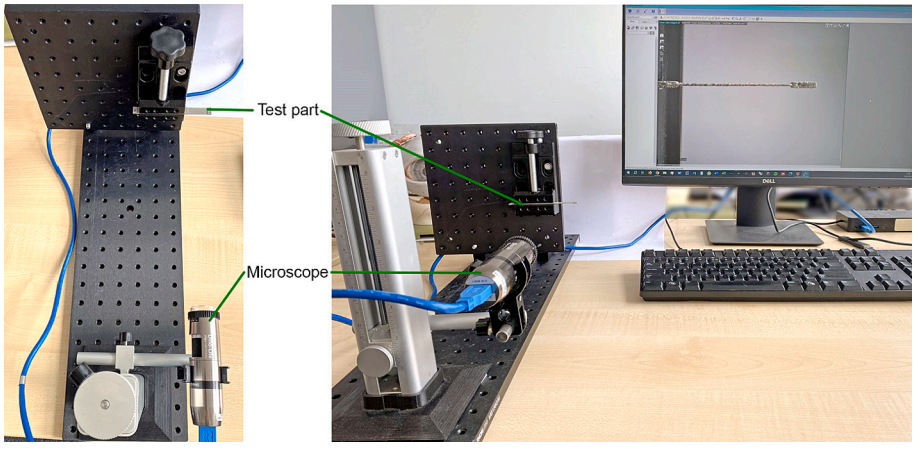

Fig. 5. Set-up used to test the deflection of the flexures. The set-up shows one of the 25 mm lattices without weights. Only one side of the test part was tested at a time, to test the 10 mm flexure, the test part was reversed in the clamp.

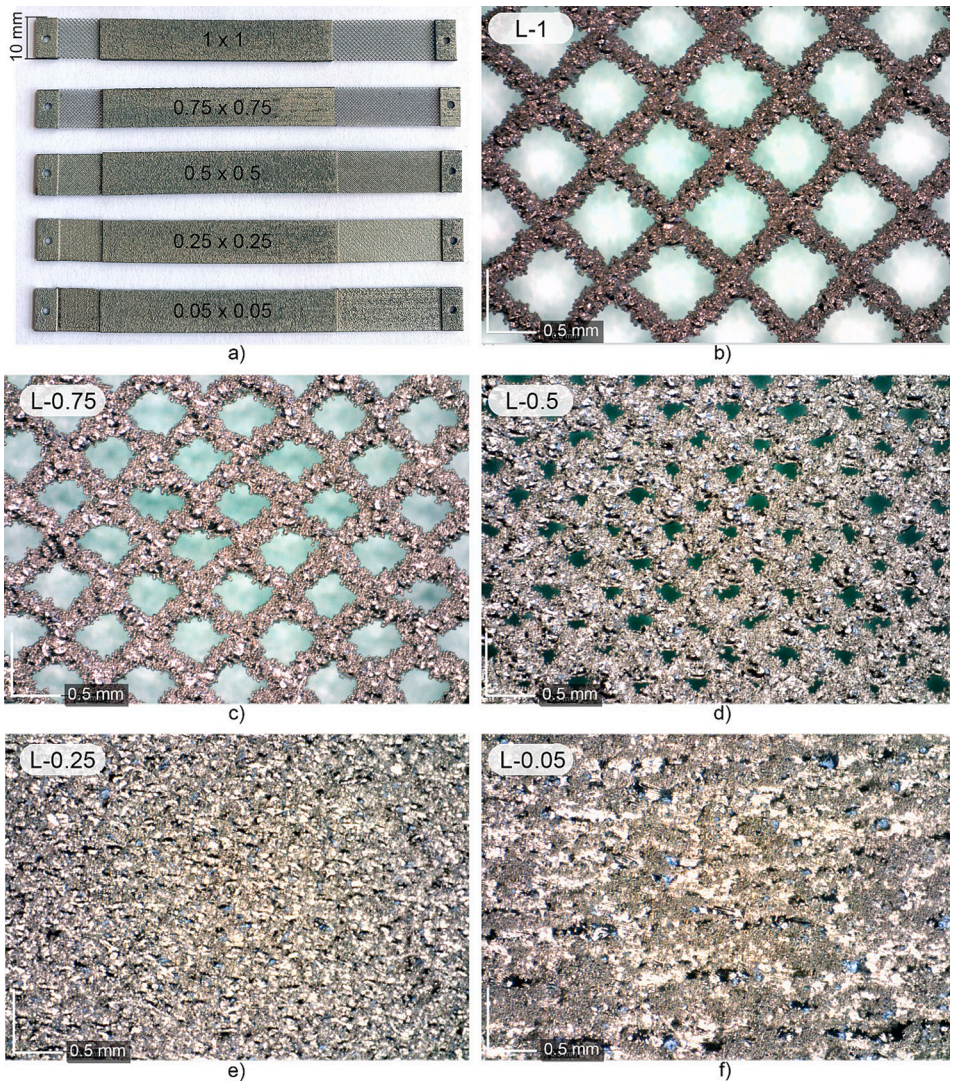

Fig. 6. Results of the printed lattice flexures. a) Printed test strips. b) Close up of L-1 lattice. c) Close up of L-0.75 lattice. d) Close up of L-0.5 lattice. e) Close up of L-0.25 lattice. f) Close up of L-0.05 lattice.

Table 2
Results of the dimensional measurements of the different lattice types.

	L-1	L-0.75	L-0.5	L-0.25	L-0.05
Lattice size	1 × 1	0.75 × 0.75	0.5 × 0.5	0.25 × 0.25	0.05 × 0.05
Wall thickness (mm)	0.26	0.26	0.26	0.26	0.54
Strut size (mm) (n = 4)	0.20 ± 0.01	0.23 ± 0.01	0.19 ± 0.01	–	–
Theoretical porosity (g)*	0.087	0.110	0.150	0.207	0.444
Actual porosity (g)*	0.067	0.073	0.130	0.170	0.360

*For the 25 mm lattice.

The wall thickness of all lattices up to L-0.25 is 0.26 mm on average, while the wall thickness of L-0.05 is 0.54 mm, similar to the thickness of a solid wall (0.55 mm). It is noticeable that although the pattern, as well as the 'openness', of L-0.25 and L-0.05 seems similar under the microscope, the wall thickness of L-0.05 is approximately twice as large. The average strut sizes of L-1, L-0.75, and L-0.5 are approximately 0.20 mm, for the other lattice sizes, no separate struts could be discerned. The theoretical and actual porosity of the lattices, as given in Table 1, shows that the porosity of the printed samples is significantly lower for all lattice structures. It should be noted that the same strut size of 0.20 mm was used to calculate the theoretical porosity for all lattices, meaning that L-0.05 was modeled with a wall thickness more than twice as low as the printed lattice.

The results of the deflection test are shown in Fig. 7a-b. As was expected, the L-1 lattices show the lowest bending stiffness and deflect the most under the applied force. The 10 mm and 25 mm L-1 showed a maximum slope under a 100 g load of 74.1° and 87.6°, respectively. One of the 25 mm L-1 mm strips broke off at the connection points when applying the mass of 100 g. The L-0.75 lattices were more fragile than the L-1 lattices: all three of the 10 mm L-0.75 lattices broke; two at a load of 30 g and one at a load of 80 g. This is likely due to geometrical imperfections or print defects [40], although none could be detected before the test.

In Fig. 7a-b it can be seen that the slope of the L-0.75 lattices is closer to the L-1 lattices than the L-0.5 lattices. There appears to be little difference in flexibility for the L-1 versus the L-0.75 lattices. The L-0.05 lattices show hardly any deflection, with slope angles of 1.6° for the 10 mm lattice and 9.5° for the 25 mm lattice. The 10 mm L-0.05 did not show any deflection until 80 g of load was applied. In Fig. 7c-d the deflection of one L-1 and one L-0.25 is shown for both flexure lengths and all loads. L-0.25 showed 77 % less deflection for the 10 mm and 39

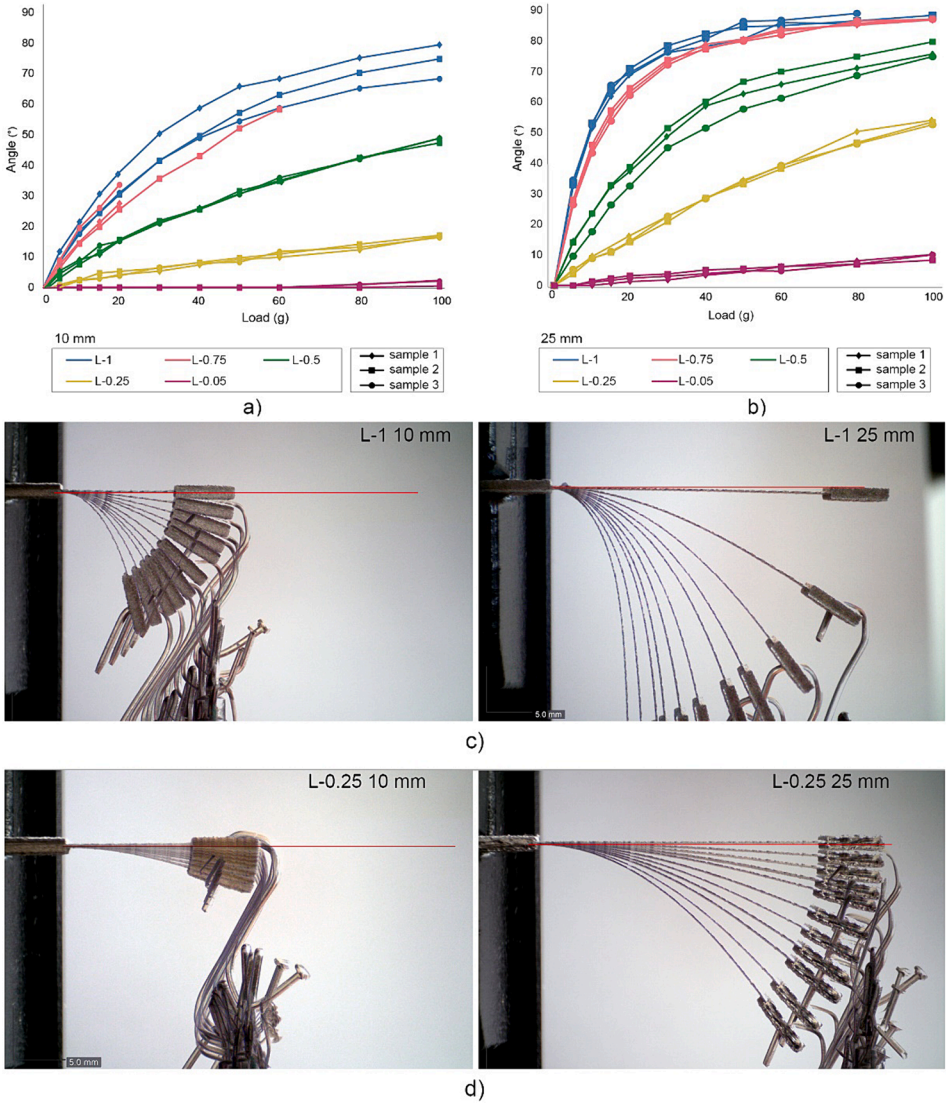

Fig. 7. Results from the deflection tests for the 10 mm flexures and 25 mm flexures. a) Slopes of the 10 mm lattices (n = 3). b) Slopes of the 25 mm lattices (n = 3). c) Combined images of the deflection tests for the L-1 lattice 10 mm (left) and 25 mm (right). d) Combined images of the deflection tests for the L-0.25 lattice 10 mm (left) and 25 mm (right).

% less deflection for the 25 mm length as compared to L-1. It was noticeable that for all lattices, except for L-0.05, the lattices had plastically deformed after removal of the 100 g load, with as much as a 9° residual angle for the 25 mm L-1.

In conclusion, the larger, less dense lattice sizes resulted in more flexibility but were also more fragile and more difficult to print consistently. We observed no difference in lattice structure between L-0.25 and L-0.05 concerning openness or print quality. Nonetheless, the wall

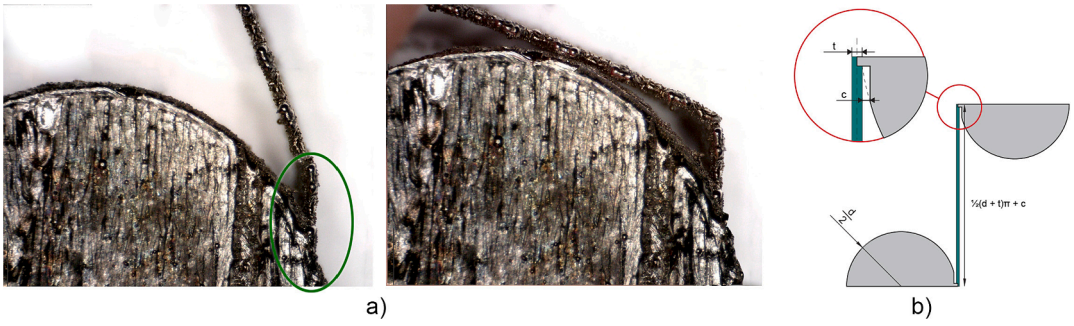

Fig. 8. One of the failed joint batches and the redesign. a) A microscope close up of one of the joints, showing that the lattice is partially fused to the joint body, indicated by the green circle. b) The lattice breaks when attempting to bend it over the joint body. c) Redesign to prevent fusing of the lattice to the joint body, in which the lattice with thickness t is placed more to the side of the joint and a clearance c is added. (For interpretation of the references to colour in this figure legend, the reader is referred to the web version of this article.)

thickness of the L-0.05 lattice is twice as much as the L-0.25 lattice, resulting in a high-stiffness flexure. Therefore, lattice sizes larger than L-0.25 are to be recommended for our purpose. Although the lattices are somewhat fragile, most can withstand at least 1 N of transverse force.

3.2. Rolling joints

The lattices of the joints in the batch that received the heat treatment became too brittle and broke off when bending. Therefore, the heat treatment was omitted for the following batches. In the subsequent batch, it was found that the lattices had fused to the joint body over a distance of approximately 1.5 mm, causing them to break at this location (Fig. 8a-b). Therefore, for the third batch, we altered the design to incorporate the thickness of the lattice into the joint, as well as a clearance, as shown in Fig. 8c, in which *d* is the joint diameter of 5 mm, 7.5 mm, or 10 mm, *t* the lattice thickness of 0.26 mm, and *c* the clearance value of 0.15 mm. This design ensured that the flexure was able to lay flat across the surface of the body without fusing.

During removal with wire EDM, most of the L-1 lattices broke at the attachment point, except for one 10 mm joint. For the remaining joints, of which a few examples are illustrated in Fig. 9a, it was possible to curve the lattice over the joint body, indicating that the bending radius of the lattices corresponded to the joint size. However, when connecting the two joint parts the majority of the lattices broke at different places along the length of the lattice (Fig. 9b).

The joints that were assembled successfully were the 10 mm diameter joints with L-0.5 and L-0.25 lattice; the 7.5 mm diameter joint with L-0.5 and L-0.25 lattice; and the 5 mm diameter joint with L-0.25 lattice (Fig. 9c). All of them show a slight deformation in the form of twisting of the joint. All five assembled joints were able to bend up to 90° in both directions (Fig. 9d-e). Once assembled, the joints were stable and did not show signs of breakage for at least 100 times bending. A difference in stiffness was clearly noticeable between the joints, the 5 mm diameter joint required more force to move than the larger joints, and the L-0.25 lattice required more force than the L-0.5 lattice.

For the rolling joint, we explored two variable design parameters: the joint size and the lattice structure. Reducing the joint size reduces the length of the flexure, increases the stiffness of the flexure, and reduces the height of the joint, which reduces the number of attachment points of the lattice to the joint. The latter is illustrated in Fig. 10. A lower number of attachment points increases the fragility of the connection. This effect was especially noticeable in the joints printed with the L-1 lattices, which fractured at the attachment of the lattice to the joint. Increasing the lattice grid size decreases the stiffness of the flexure, but reduces the number of attachment points. A balance between joint size and lattice structure must be found to produce the smallest joints with the lowest stiffness while maintaining a sufficiently strong connection.

Bending radii of 10 mm, 7.5 mm, and 5 mm were feasible for all lattice grid sizes. However, only the stiffer lattices, L-0.5 and L-0.25, remained intact when assembling the joint halves. The 5 mm diameter joint was only functional with the stiffest L-0.25 lattice, although the resulting joint had a high bending stiffness and was therefore found unsuitable to apply in a steerable instrument. Since the working of the lattices seems to be optimal when the joints are not assembled, i.e. the lattice is not forced into a pre-tensioned position, in the next section for the instrument design we explore the use of single-layer rolling joints with a different lattice configuration that does not require assembly or pre-tensioning of the flexures.

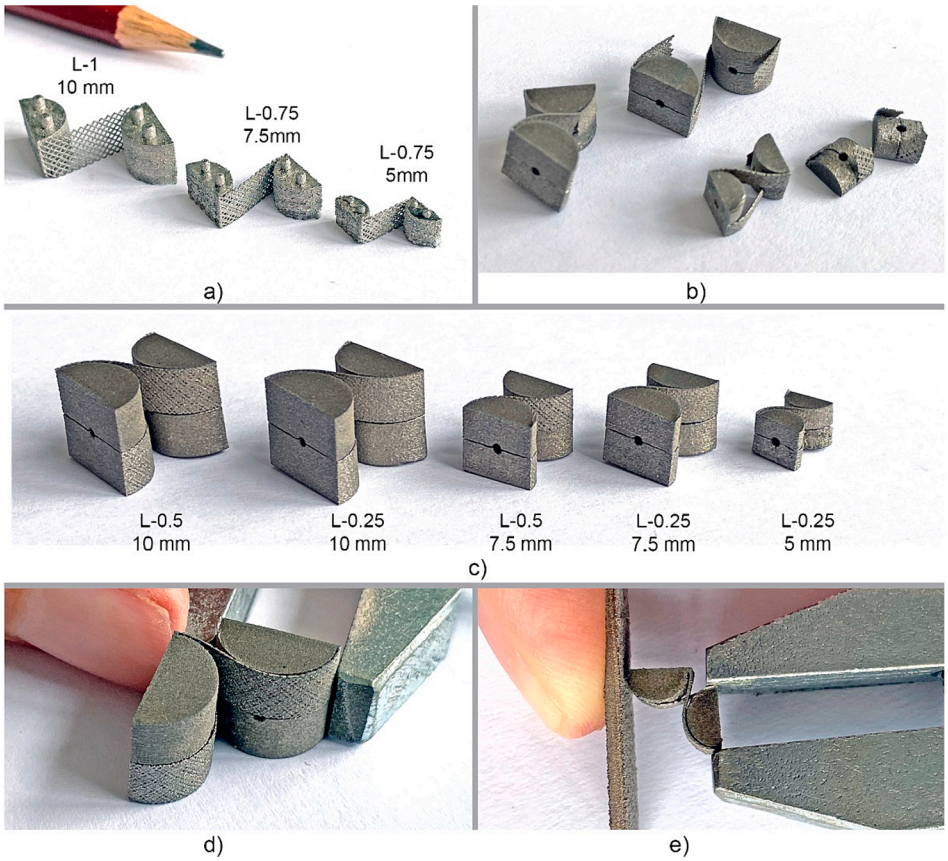

Fig. 9. 3D printed rolling contact joints. a) Single 3D printed joint halves. b) Some of the broken assembled joints. c) The successfully assembled joints. d) The 10 mm L-0.5 joint illustrating a bending angle of 90°. e) The 5 mm L-0.25 joint illustrating a bending angle of 90°.

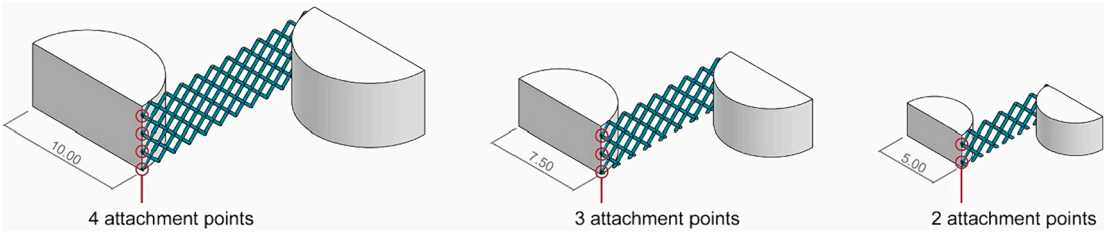

Fig. 10. Effects of decreasing the joint size. When decreasing the size of the joint with a constant lattice size, the number of attachment points from the lattice to the joint also decreases, which can lead to a fragile connection.

4. Instrument design and manufacture

4.1. Joint configuration and actuation

Actuation of the instrument without relying on cables can be implemented by for instance making use of ribbons [12], thin rigid rods [45,46], or multi-linkage systems with rigid body joints [47,48]. As both ribbon actuation and multi-linkage systems are prone to sliding friction during actuation, we settled on using rigid rods to actuate the steering and the grasper. The schematic design and working principle of the instrument are shown in Fig. 11. In this design, two pairs of rolling joints are placed next to each other with the flexures in a straight configuration. By applying an inwards force to the handle, the flexures roll over the circular joint and transfer the motion through the rigid rods to the grasper. The joints have been given a diameter of 5 mm, with rods of 1 mm thickness, resulting in a total width of 15.5 mm. The height of the entire instrument is 5 mm, which gives the lattices sufficient attachment points to the joint and the shaft. The grasper is printed in its open position with jaws in a 30° angle. To obtain a 45° steering angle, the largest rotation for each grasper jaw results in a 75° rotation (Fig. 11). The length of the flexure is calculated based on the arc length on the surface of the joint diameter for this angle, given by $\pi(d+\frac{t}{2}) \bullet \frac{75}{360}$, which equals 3.4 mm. To ensure sufficient flexibility of the flexures, we increased this length to 5 mm.

4.2. 3D printed prototypes

The initial prototype of the design, employing L-1 lattices (Fig. 12a), revealed two issues. First, upon rotation, the stiffness of the flexures caused an outward displacement of the outer rods (Fig. 12a). Second, despite the intended 1:1 motion transfer, the prototype's grasper was unable to fully close. To address this, we enlarged the joints at the handle from 5 mm to 7.5 mm, amplifying handle movement and ensuring complete grasper closure during actuation (Fig. 12b).

To prevent the outward movement of the rods, we considered reducing the flexure stiffness or mechanically securing the rods. We opted for the latter, which requires a mechanical connection allowing the outer rods to move relative to each other and the inner rod. This connection is longitudinally flexible yet laterally rigid. To achieve this, while fulfilling our requirements regarding assembly and post-processing, we implemented a linear compliant mechanism using lattice flexures connecting the outer rods to the inner rod. For small displacements, as is the case in our design, this compliant mechanism facilitates unidirectional motion. In addition, to reduce the stiffness of the flexures, we enhanced their slenderness by utilizing the instrument's full width, which involved changing the rod shape from straight to 'meandering' (Fig. 12b).

The adjusted design was printed two times, again with lattices of L-1 (Fig. 13a). The total printing time was approximately 6 h. When removing the prototype from the build plate using wire EDM, stresses within the material caused significant deformation of the grasper and handles, as shown in Fig. 13b. This deformation caused torsion of the flexures. Both prototypes functioned for a short time, as can be seen in Supplementary Video 1 (available through DOI: 10.4121/cd5d1e9d-7c34-45ec-b081-94db60b43477), but after a few manipulations, the lattices at the grasper side failed. This time, the grasper was able to

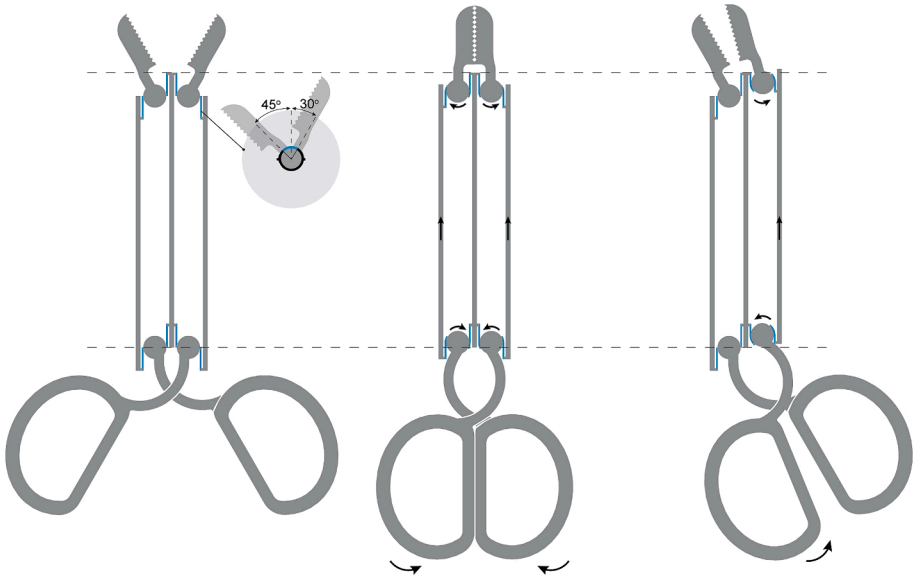

Fig. 11. Working principle of the non-assembly steerable instrument, in which the flexures are indicated in blue, showing the neutral position (left), closing of the grasper (middle), and steering of the grasper from the neutral position (right). The grey dashed lines show the position of the middle rod. (For interpretation of the references to colour in this figure legend, the reader is referred to the web version of this article.)

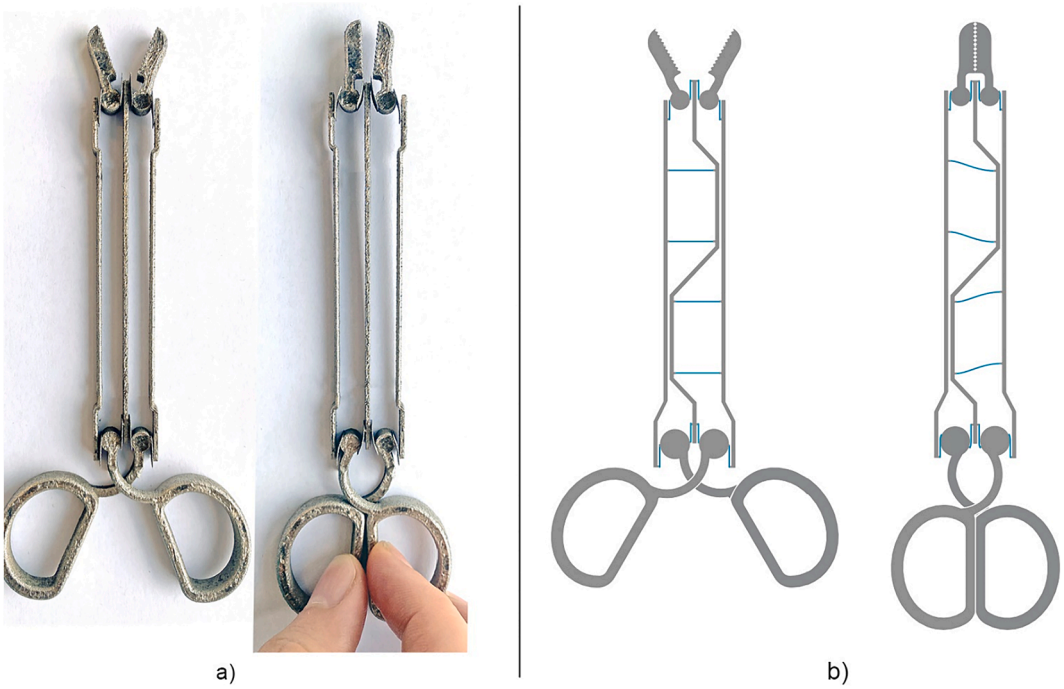

Fig. 12. First 3D printed prototype and design iteration. a) The 3D printed prototype in open (left) and closed (right) position. In the closed position it can be seen that the outer rods are pushed outwards, and that the grasper does not fully close. b) Adjusted design of the non-assembly instrument, in which a linear compliant mechanism was added to prevent the rods from moving outwards, and the joints near the handle have been increased in size. The top shows the grasper in neutral position, and the bottom shows the closing of the grasper and deformation of the compliant flexures.

fully close (Fig. 13c). However, the outer rods show clear deformation towards the distal end, indicating they are still being forced outwards when actuating the grasper. The desired steering angle of 45° of the grasper could not be obtained, no more than 20° was possible before the lattices started to fail.

5. Evaluation and discussion

5.1. Flexures and joints

This article explores the possibility of designing a completely non-assembly steerable surgical instrument using SLM printing with titanium. Due to the rough surface finish of SLM printed parts, which can interfere with the motion of mechanical parts, negating the advantages of non-assembly instruments by requiring extensive surface treatments to function, we attempted to design a low friction instrument that is not hindered by the rough surface finish. To do so, we explored the possibility of 3D printing compliant flexures with a lattice structure, to reduce the stiffness and miniaturize the instrument. We succeeded in printing various lattice designs with differences in stiffness, by which we reduced the minimum printed wall thickness to 0.26 mm (approximately 50 % of the regular minimum wall thickness), to achieve low stiffness flexures. We found there is a fine line between printability and functionality; the lattices are very sensitive to print parameters, and factors such as the location on the build plate and total volume of the parts can affect the results.

The difference in wall thickness between L-0.05 and the other lattice sizes likely stems from the fact that the cell size of this lattice is smaller than the laser spot size (0.05 × 0.05 versus 0.073 mm, excluding melt pool). Since one voxel is printed for each layer height, which is also 0.05 mm, there is significant overlap between the printed voxels and we hypothesize that this increases the melt pool surrounding the voxels, resulting in an increased wall thickness. We have not specifically investigated the behavior of lattices with grid sizes between 0.25 × 0.25 mm and 0.05 × 0.05 mm in this study, however, future studies to investigate the minimum grid size that results in a wall thickness of approximately 0.25 mm could contribute to the knowledge and understanding of lattice flexures.

Miniaturization of the flexures results in contradictory requirements. Since the minimum wall thickness remains a fixed value, reducing the gird size of the lattice leads to an increase in stiffness. This can be solved by a reduction in material in the form of a larger lattice size, although this makes for an increasingly fragile flexure. This, in turn, can be somewhat mitigated by increasing the height of the lattice. Alternatively, the design of lattices with variable grid sizes, in which a denser grid is applied towards the edges to maximize the number of attachment points, can be explored [49].

A rolling joint is advantageous considering the fragility of the lattice structures, since the bending angle of the lattice is confined by the solid portion of the joint, limiting sharp bending angles and preventing breakage. Although we have demonstrated that it is possible to 3D print functional rolling joints in different sizes, some downsides are making it less feasible to apply in a non-assembly instrument. Since it is only possible to print the lattices in a straight configuration, they cannot be produced completely non-assembly, and bending of the lattices results in significant stress. Ideally, for torsion stiffness and joint stability, the joint should consist of at least three layers of crossed flexures in alternating directions instead of two, making it more complicated to produce non-assembly. However, for applications where size and assemblability are not of concern, the rolling joint can be a suitable solution for a low-friction SLM joint that can be 3D printed in different scales.

5.2. Instrument design improvements

We incorporated an alternative design of a traditional rolling joint in the steerable instrument, which increased compatibility with the drawn-up requirements. Although the instrument was functional, the lattices only lasted for a short time before breaking. The main reason for this were the significant stresses present in the material that caused substantial deformation of the grasper and handle, leading to warping of the

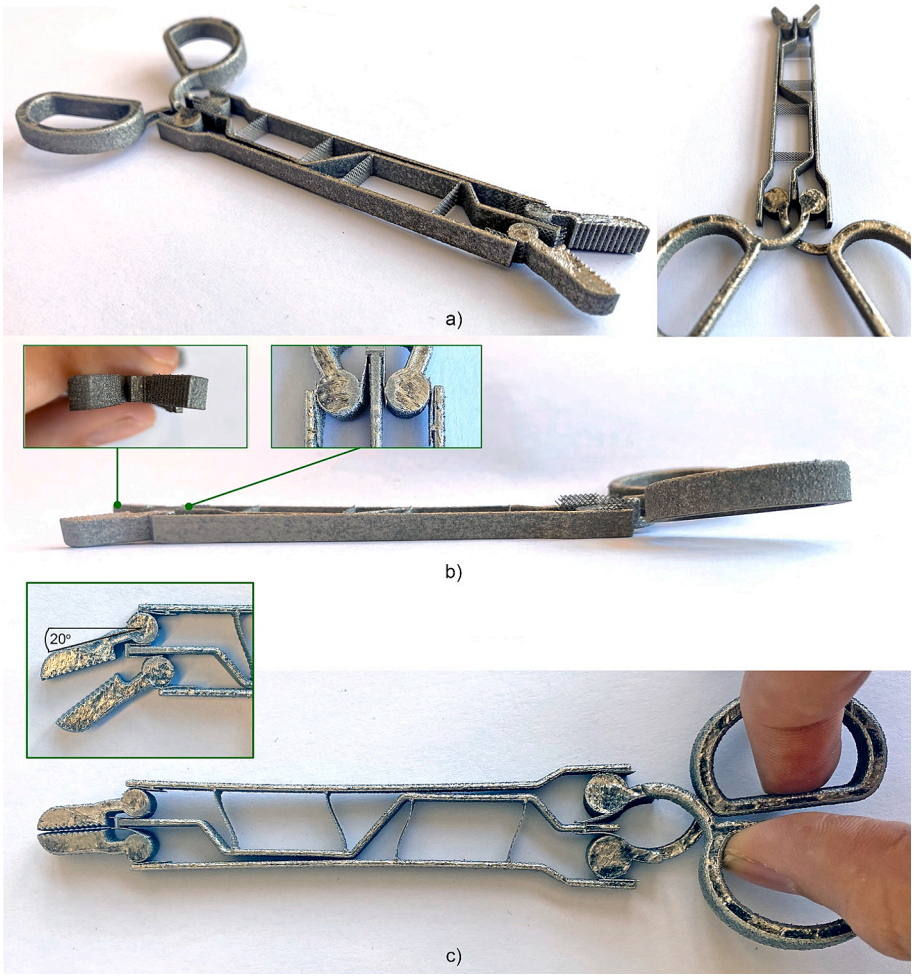

Fig. 13. Second iteration of the 3D printed prototype. a) 3D printed prototype. b) Side view of the prototype, showing clear warpage in the handle, and close ups of the warpage in the grasper as well as the torsion in the flexures. c) Closing of the grasper was possible with this prototype, although deformation of the outer rods is visible. The grasper was able to bend 20°.

flexures. Usually, these stresses are mitigated by applying a heat treatment immediately after printing, however, this resulted in brittle lattices. Subsequent studies could explore the parameters of heat treatments to reduce stresses while maintaining lattice flexibility, as it has been shown that heat treatments provide the possibility of tuning the mechanical properties, although the relationship between different settings is not yet well understood [41].

The instrument design can further be improved by elongating the flexures of the rolling joints, further increasing the flexibility. This might also prevent the deformation in the outer rods caused by the inherent bending stiffness of the flexures. At the handle side, the height of the joints can be raised to increase the attachment points for the lattice. In the prototypes in Figs. 12-13, the length of the shaft was adjusted to the size of the build plate, however with a larger build plate the length can be increased. In that case, we suggest adding more meanders and flexures to the middle rod to retain the position of the outer rods. In order to miniaturize the width of the total instrument, the radius of the rolling joints would need to decrease, which is in practice limited by the minimum bending radius of the flexures. More research is necessary to determine this minimum radius. With the current lattice structure and SLM printer used in this study, we speculate that it is not possible to decrease the diameter to less than 5 mm, unless the wall thickness of the lattices can be reduced further. Alternatively, the design can be adjusted so that only one half of the grasper is steerable, and the other half is stationary.

It should be noted that although titanium can withstand the temperature required for sterilization, in practice the rough porous surface is challenging to sterilize, can potentially damage tissue, and risks leaving particles behind during the surgery. A solution for clinical implementation could be adding a flexible sleeve of a biocompatible material around the instrument.

5.3. *Design process*

Usually in a standard design process, first a design is drawn up, after which a specific production process is chosen and the design is adjusted to its specifications. However, in the case of AM, an incredible amount of design freedom can be obtained which can be difficult to comprehend for designers. In this study, we demonstrated a different approach towards designing for AM. We started with an analysis of the production method, in this case SLM, and attempted to expand its boundaries to generate a completely new design. Without a thorough analysis of the printer parameters, the non-assembly design that we have presented would not have been contrived, which is why this can be considered a 3D printer-driven design process. There are some caveats to this method, as the current design is adjusted to the conditions of one specific printer. The type of SLM printer that we used is in general suitable for large parts, but less suited for miniature work such as in this study. With a printer suitable for small parts, better results can be obtained, and more design directions can be explored. Nonetheless, the design process presented here shows the potential of designing at the limits of the production boundaries.

6. Conclusion

This study explored the feasibility of designing a non-assembly steerable surgical instrument using SLM printing. The rough surface finish of SLM printed parts poses challenges in creating functional non-assembly instruments, requiring extensive surface treatments. Therefore, we attempted to design a low-friction instrument that is not hindered by the rough surface finish of SLM. We explored the possibility of 3D printing compliant flexures with a lattice structure, to reduce the stiffness of the flexures and miniaturize the instrument. Various lattices with grid sizes ranging from 1 mm to 0.05 mm were successfully printed, and we succeeded in reducing the thickness of the flexures from 0.55 mm with regular print settings, to 0.26 mm with lattice design. The lattices were applied in the design of rolling joints with crossed, curved flexures in 10 mm, 7.5 mm, and 5 mm diameters. We showed that all lattice grid sizes were able to obtain a bending radius of at least 5 mm and that the larger grid sizes have lower bending stiffness than the smaller lattice sizes. The number of attachment points of the lattice to the joint body was found to be important, since this determines the fragility of the connection. For the 5 mm joints, this means that using a large lattice size to reduce the flexure stiffness often results in joint failure, due to the low number of attachment points. The pre-tensioning of the lattices in the rolling joints led to breakage of the lattices, therefore in the instrument design we explored the use of rolling joints with straight flexures that did not require pre-tensioning, and as such do not require assembly. The resulting steerable instrument is completely non-assembly, and specifically adjusted to the parameters of the SLM process. We showed the potential of the design through several prototypes, although the fragility of the lattices limited their longevity. Further research and development are needed to enhance the durability of lattice-based instruments for clinical applications.

Funding

This project has received funding from the Interreg 2 Seas programme 2014–2020 co-funded by the European Regional Development Fund under subsidy contract No. 2S04-014.

CRediT authorship contribution statement

Kirsten Lussenburg: Writing – review & editing, Writing – original draft, Visualization, Validation, Software, Methodology, Investigation, Formal analysis, Data curation, Conceptualization. **Remi van Starkenburg:** Writing – review & editing, Software, Investigation, Conceptualization. **Aimée Sakes:** Writing – review & editing, Supervision. **Paul Breedveld:** Writing – review & editing, Supervision, Funding acquisition, Conceptualization.

Declaration of competing interest

The authors declare that they have no known competing financial interests or personal relationships that could have appeared to influence the work reported in this paper.

Data availability

Data will be made available on request.

Appendix A. Supplementary data

Supplementary data to this article can be found online at https://doi.org/10.1016/j.matdes.2024.112845.

References

[1] C. Culmone, G. Smit, P. Breedveld, Additive manufacturing of medical instruments: A state-of-the-art review, Addit. Manuf. 27 (2019) 461–473, https://doi.org/10.1016/j.addma.2019.03.015.
[2] P. Tack, J. Victor, P. Gemmel, L. Annemans, 3D-printing techniques in a medical setting: a systematic literature review, Biomed. Eng. Online 15 (2016) 115, https://doi.org/10.1186/s12938-016-0236-4.
[3] K. Lussenburg, A. Sakes, P. Breedveld, Design of non-assembly mechanisms: A state-of-the-art review, Addit. Manuf. 39 (2021) 101846, https://doi.org/10.1016/j.addma.2021.101846.
[4] L.F. Velásquez-García, Y. Kornbluth, Biomedical applications of metal 3D printing, Annu. Rev. Biomed. Eng. 23 (2021) 307–338, https://doi.org/10.1146/annurev-bioeng-082020-032402.
[5] C.A. Seneci, J. Shang, A. Darzi, G.-Z. Yang, Rapid manufacturing with selective laser melting for robotic surgical tools: Design and process considerations, in: 2015 IEEE/RSJ International Conference on Intelligent Robots and Systems (IROS), IEEE, 2015: pp. 824–830. doi: 10.1109/IROS.2015.7353467.
[6] F.S.L. Bobbert, K. Lietaert, A.A. Eftekhari, B. Pouran, S.M. Ahmadi, H. Weinans, A. A. Zadpoor, Additively manufactured metallic porous biomaterials based on minimal surfaces: A unique combination of topological, mechanical, and mass transport properties, Acta Biomater. 53 (2017) 572–584, https://doi.org/10.1016/j.actbio.2017.02.024.
[7] S.L. Sing, J. An, W.Y. Yeong, F.E. Wiria, Laser and electron-beam powder-bed additive manufacturing of metallic implants: A review on processes, materials and designs, J. Orthop. Res. 34 (2016) 369–385, https://doi.org/10.1002/jor.23075.
[8] S. Nahata, O.B. Ozdoganlar, Feasibility of metal additive manufacturing for fabricating custom surgical instrumentation for hip and knee implants, Procedia Manuf. 34 (2019) 772–779, https://doi.org/10.1016/j.promfg.2019.06.207.
[9] R. Singh, A. Suri, Three-dimensional printed ergonomically improved microforceps for microneurosurgery, World Neurosurg. 141 (2020) e271–e277, https://doi.org/10.1016/j.wneu.2020.05.105.
[10] R. Kontio, Designing and additive manufacturing a prototype for a novel instrument for mandible fracture reduction, surgery, Curr. Res. 03 (2013) 2–4, https://doi.org/10.4172/2161-1076.S1-002.
[11] S.M. Fuller, D.R. Butz, C.B. Vevang, M.V. Makhlouf, Application of 3-dimensional printing in hand surgery for production of a novel bone reduction clamp, J. Hand Surg. Am. 39 (2014) 1840–1845, https://doi.org/10.1016/j.jhsa.2014.06.009.
[12] A. Sakes, K. Hovland, G. Smit, J. Geraedts, P. Breedveld, Design of a novel three-dimensional-printed two degrees-of-freedom steerable electrosurgical grasper for minimally invasive surgery, J. Med. Devices 12 (2018) 011007, https://doi.org/10.1115/1.4038561.
[13] C.A. Seneci, G. Gras, P. Wisanuvej, J. Shang, G.-Z. Yang, 3D printing of improved needle grasping instrument for flexible robotic surgery, in: 2017 IEEE/RSJ International Conference on Intelligent Robots and Systems (IROS), IEEE, 2017: pp. 2524–2530. doi: 10.1109/IROS.2017.8206072.
[14] Y. Hu, L. Zhang, W. Li, G.-Z. Yang, Design and fabrication of a 3-D printed metallic flexible joint for snake-like surgical robot, IEEE Rob. Autom. Lett. 4 (2019) 1557–1563, https://doi.org/10.1109/LRA.2019.2896475.
[15] S. Coemert, M.F. Traeger, E.C. Graf, T.C. Lueth, Suitability evaluation of various manufacturing technologies for the development of surgical snake-like manipulators from metals based on flexure hinges, Procedia CIRP 65 (2017) 1–6, https://doi.org/10.1016/j.procir.2017.03.108.
[16] M. Hanief, M.F. Wani, Effect of surface roughness on wear rate during running-in of En31-steel: model and experimental validation, Mater. Lett. 176 (2016) 91–93, https://doi.org/10.1016/j.matlet.2016.04.087.
[17] L. Löber, C. Flache, R. Petters, U. Kühn, J. Eckert, Comparison of different post processing technologies for SLM generated 316l steel parts, Rapid Prototyp J. 19 (2013) 173–179, https://doi.org/10.1108/13552541311312166.
[18] K. Lussenburg, R. van Starkenburg, M. Bruins, A. Sakes, P. Breedveld, Polishing of metal 3D printed parts with complex geometry: Visualizing the influence on geometrical features using centrifugal disk finishing, PLoS One 18 (2023) e0289730, https://doi.org/10.1371/journal.pone.0289730.
[19] S. Bagehorn, J. Wehr, H.J. Maier, Application of mechanical surface finishing processes for roughness reduction and fatigue improvement of additively manufactured Ti-6Al-4V parts, Int. J. Fatigue 102 (2017) 135–142, https://doi.org/10.1016/j.ijfatigue.2017.05.008.
[20] C. Culmone, P.W.J. Henselmans, R.I.B. van Starkenburg, P. Breedveld, Exploring non-assembly 3D printing for novel compliant surgical devices, PLoS One 15 (2020) e0232952, https://doi.org/10.1371/journal.pone.0232952.
[21] C. Culmone, K. Lussenburg, J. Alkemade, G. Smit, A. Sakes, P. Breedveld, A fully 3D-printed steerable instrument for minimally invasive surgery, Materials 14 (2021) 7910, https://doi.org/10.3390/ma14247910.
[22] N.P. Castledine, J.H. Boyle, J. Kim, Design of a modular continuum robot segment for use in a general purpose manipulator, in: 2019 International Conference on Robotics and Automation (ICRA), IEEE, 2019: pp. 4430–4435. doi: 10.1109/ICRA.2019.8794249.
[23] B.V. Johnson, Z. Gong, B.A. Cole, D.J. Cappelleri, Design of Disposable 3D printed surgical end-effectors for robotic lumbar discectomy procedures, in: Volume 5A: 42nd Mechanisms and Robotics Conference, American Society of Mechanical Engineers, 2018, https://doi.org/10.1115/DETC2018-85257.
[24] D.B. Roppenecker, A. Pfaff, J.A. Coy, T.C. Lueth, Multi arm snake-like robot kinematics, in: 2013 IEEE/RSJ International Conference on Intelligent Robots and Systems, IEEE, 2013: pp. 5040–5045. doi: 10.1109/IROS.2013.6697085.
[25] S.N. Economidou, M.J. Uddin, M.J. Marques, D. Douroumis, W.T. Sow, H. Li, A. Reid, J.F.C. Windmill, A. Podoleanu, A novel 3D printed hollow microneedle

microelectromechanical system for controlled, personalized transdermal drug delivery, Addit. Manuf. 38 (2021) 101815, https://doi.org/10.1016/j.addma.2020.101815.
[26] J. Jiang, X. Xu, J. Stringer, Support structures for additive manufacturing: a review, J. Manuf. Mater. Process. 2 (2018) 64, https://doi.org/10.3390/jmmp2040064.
[27] F. Gutmann, M. Stilz, S. Patil, F. Fischer, K. Hoschke, G. Ganzenmüller, S. Hiermaier, Miniaturization of non-assembly metallic pin-joints by LPBF-based additive manufacturing as perfect pivots for pantographic metamaterials, Materials 16 (2023) 1797, https://doi.org/10.3390/ma16051797.
[28] J. Kranz, D. Herzog, C. Emmelmann, Design guidelines for laser additive manufacturing of lightweight structures in TiAl6V4, J. Laser Appl. 27 (2015) S14001, https://doi.org/10.2351/1.4885235.
[29] Y. Liu, J. Zhang, Y. Yang, J. Li, J. Chen, Study on the influence of process parameters on the clearance feature in non-assembly mechanism manufactured by selective laser melting, J. Manuf. Process. 27 (2017) 98–107, https://doi.org/10.1016/j.jmapro.2017.04.005.
[30] F. Calignano, D. Manfredi, E.P. Ambrosio, S. Biamino, M. Pavese, P. Fino, Direct fabrication of joints based on direct metal laser sintering in aluminum and titanium alloys, Procedia CIRP. 21 (2014) 129–132, https://doi.org/10.1016/j.procir.2014.03.155.
[31] M.A.A. Leeflang, F.S.L.S.L. Bobbert, A.A.A. Zadpoor, Additive manufacturing of non-assembly deployable mechanisms for the treatment of large bony defects, Addit. Manuf. 46 (2021) 102194, https://doi.org/10.1016/j.addma.2021.102194.
[32] A. Jeanneau, J. Herder, T. Laliberté, C. Gosselin, A compliant rolling contact joint and its application in a 3-DOF planar parallel mechanism with kinematic analysis, in: Volume 2: 28th Biennial Mechanisms and Robotics Conference, Parts A and B, 2004, pp. 689–698, https://doi.org/10.1115/DETC2004-57264.
[33] P.A. Halverson, L.L. Howell, S.P. Magleby, Tension-based multi-stable compliant rolling-contact elements, Mech. Mach. Theory 45 (2010) 147–156, https://doi.org/10.1016/j.mechmachtheory.2008.11.013.
[34] J.W. Suh, K.Y. Kim, J.W. Jeong, J.J. Lee, Design considerations for a hyper-redundant pulleyless rolling joint with elastic fixtures, IEEE/ASME Trans. Mechatron. 20 (2015) 2841–2852, https://doi.org/10.1109/TMECH.2015.2389228.
[35] J.P. Kuntz, Rolling Link Mechanisms, 1995.
[36] D. Zhang, Y. Sun, T.C. Lueth, Design of a novel tendon-driven manipulator structure based on monolithic compliant rolling-contact joint for minimally invasive surgery, Int. J. Comput. Assist. Radiol. Surg. 16 (2021) 1615–1625, https://doi.org/10.1007/s11548-021-02442-w.
[37] Y. Sun, T.C. Lueth, Cruciate-ligament-inspired compliant joints: Application to 3D-printed continuum surgical robots, in: 2021 43rd Annual International Conference of the IEEE Engineering in Medicine & Biology Society (EMBC), IEEE, 2021: pp. 4645–4648. doi: 10.1109/EMBC46164.2021.9630239.
[38] P. Berthet-Rayne, K. Leibrandt, K. Kim, C.A. Seneci, J. Shang, G.-Z. Yang, Rolling-joint design optimization for tendon driven snake-like surgical robots, in: 2018 IEEE/RSJ International Conference on Intelligent Robots and Systems (IROS), 2018, pp. 4964–4971, https://doi.org/10.1109/IROS.2018.8593517.
[39] Z. Wu, S.P. Narra, A. Rollett, Exploring the fabrication limits of thin-wall structures in a laser powder bed fusion process, Int. J. Adv. Manuf. Technol. 110 (2020) 191–207, https://doi.org/10.1007/s00170-020-05827-4.
[40] T. Maconachie, M. Leary, B. Lozanovski, X. Zhang, M. Qian, O. Faruque, M. Brandt, SLM lattice structures: Properties, performance, applications and challenges, Mater. Des. 183 (2019) 108137, https://doi.org/10.1016/j.matdes.2019.108137.
[41] E.G. Merriam, L.L. Howell, Lattice flexures: Geometries for stiffness reduction of blade flexures, Precis. Eng. 45 (2016) 160–167, https://doi.org/10.1016/j.precisioneng.2016.02.007.
[42] A. Jiansheng Pan, B. Jianwei Wu, C. Yin Zhang, D. Hui Wang, E. Jiubin Tan, Design and analyze of flexure hinges based on triply periodic minimal surface lattice, Precis. Eng. 68 (2021) 338–350, https://doi.org/10.1016/j.precisioneng.2020.12.019.
[43] J. Kruis, F. Cosandier, G. Perruchoud, L. Kiener, H. Saudan, 6 Design principles for SLM-based compliant mechanisms. Joint Special Interest Group Meeting between Euspen and ASPE Advancing Precision in Additive Manufacturing, European Society for Precision Engineering and Nanotechnology, 2019.
[44] Y. Zhang, J. Wu, J. Tan, Compliance model and structure optimization method based on genetic algorithm for flexure hinge based on X-lattice structure, Complexity 2021 (2021) 1–14, https://doi.org/10.1155/2021/8819422.
[45] S.F. Hardon, F. Schilder, J. Bonjer, J. Dankelman, T. Horeman, A new modular mechanism that allows full detachability and cleaning of steerable laparoscopic instruments, Surg. Endosc. 33 (2019) 3484–3493, https://doi.org/10.1007/s00464-019-06849-0.
[46] G.J.M. Tuijthof, T. Horeman, Surgical device, in Particular for Minimally Invasive Surgery, WO2014148898A1, 2014.
[47] H. Yamashita, A. Iimura, E. Aoki, T. Suzuki, T. Nakazawa, E. Kobayashi, M. Hashizume, I. Sakuma, T. Dohi, Development of endoscopic forceps manipulator using multi-slider linkage mechanisms, in: The 1st Asian Symposium on Computer Aided Surgery, 2005, pp. 201–204, https://doi.org/10.5759/jscas1999.7.127.
[48] J. Mueglitz, G. Kunad, P. Dautzenberg, B. Neisius, R. Trapp, Kinematic problems of manipulators for minimal invasive surgery, Endosc. Surg. Allied Technol. 1 (1993) 160–164.
[49] R. Wauthle, B. Vrancken, B. Beynaerts, K. Jorissen, J. Schrooten, J.-P. Kruth, J. Van Humbeeck, Effects of build orientation and heat treatment on the microstructure and mechanical properties of selective laser melted Ti6Al4V lattice structures, Addit. Manuf. 5 (2015) 77–84, https://doi.org/10.1016/j.addma.2014.12.008.